

Modeling Interaction for Segmentation of Neighboring Structures

Pingkun Yan, *Member, IEEE*, Ashraf A. Kassim, *Member, IEEE*, Weijia Shen, and Mubarak Shah, *Fellow, IEEE*

Abstract—This paper presents a new method for segmenting medical images by modeling interaction between neighboring structures. Compared to previously reported methods, the proposed approach enables simultaneous segmentation of multiple neighboring structures for improved robustness. During the segmentation process, the object contour evolution and shape prior estimates are influenced by the interactions between neighboring shapes consisting of attraction, repulsion, and competition. Instead of estimating the *a priori* shape of each structure independently, an interactive maximum *a posteriori* shape estimation method is used for estimating the shape priors by considering shape prior distribution, neighboring shapes, and image features. Energy functionals are then formulated to model the interaction and segmentation. With the proposed method, neighboring structures with similar intensities and/or textures, and blurred boundaries can be extracted simultaneously. Experimental results obtained on both synthetic data and medical images demonstrate that the introduced interaction between neighboring structures improves segmentation performance compared with other existing approaches.

Index Terms—Energy minimization, interaction model, level set, neighboring structures, segmentation, shape prior.

I. INTRODUCTION

SEGMENTATION of anatomical structures from medical images is often the first step in computer-aided diagnosis. Further analysis depends highly on the quality of the segmented structures. Although the problem of medical image segmentation has been extensively studied for many years using different methods on a wide spectrum of imaging modalities, it continues to remain a challenging problem. Besides challenges due to imaging noise and partial volume effects [1], the similarity in intensity and texture between neighboring structures complicates the task of identifying distinct boundaries between the structures.

In this paper, we present a new method that introduces interactions between neighboring contours when carrying out the segmentation process. Our approach solves the problem of seg-

menting neighboring structures with similar appearance, usually considered as a very challenging task, by using interaction between both shape contours and *a priori* shape estimates. To the best of our knowledge, no other study uses this type of interaction in a segmentation process. The development of the interaction model is inspired by the observation that radiologists segment structures with poorly defined boundaries by considering the anatomy of neighboring structures [2]. In our study, segmentation is performed by iteratively repeating two interactive operations: *contour evolution* and *maximum a posteriori shape estimation*. When evolving shape contours, the interaction consists of modeling the “forces” of *attraction*, *repulsion*, and *competition* by taking into account the relationship between object contours and their shape estimates. The attraction describes the force of drawing the organ contour toward the learned shape prior, while repulsion and competition define the actions between neighboring curves to avoid overlapping and to solve the ambiguity of which structures the voxels belong to. During the shape estimation process, instead of estimating the global shapes of each structure independently, we propose an interactive maximum *a posteriori* (MAP) shape estimation method. The shape priors are generated according to shape prior distribution, neighboring shapes, image features, and also the current evolved curves. Energy functionals are then formulated to model the interactions. Segmentation is achieved by minimizing these functionals. With the proposed approach, neighboring structures with similar intensities and/or textures, and blurred boundaries can be extracted simultaneously.

The rest of the paper is organized as follows. Section II presents a review of related studies on *a priori* shape modeling and multiphase motion computation as well as their applications to segmentation problems. In Section III, we describe the proposed model for segmenting neighboring structures in medical images using interaction between object contours and shape priors. In Section IV, implementation of the proposed model using level set method and estimation of shape priors under multiple curve evolution are described. The evaluation methods used in our experiments are described in Section V, while the experimental results are presented and discussed in Section VI. We provide our conclusions in Section VII.

II. RELATED WORK

In recent years, geometric deformable models, or level set methods [3], [4], have been applied to medical image segmentation with considerable success. Compared to the parametric deformable models, which are also known as snakes or active contours [5], geometric deformable models are more flexible

Manuscript received March 10, 2008; revised August 26, 2008 and November 12, 2008. First published January 20, 2009; current version published March 3, 2009.

P. Yan was with the Department of Electrical and Computer Engineering, National University of Singapore, Singapore 119260, Singapore. He is now with the School of Computer Science, University of Central Florida, Orlando, FL 32816 USA, and also with Philips Research North America, 345 Scarborough Road, Briarcliff Manor, NY 10510 USA.

A. A. Kassim and W. Shen are with the Department of Electrical and Computer Engineering, National University of Singapore, Singapore 119260, Singapore (e-mail: ashraf@nus.edu.sg).

M. Shah is with the School of Computer Science, University of Central Florida, Orlando, FL 32816 USA.

Color versions of one or more of the figures in this paper are available online at <http://ieeexplore.ieee.org>.

Digital Object Identifier 10.1109/TITB.2008.2010492

due to the implicit shape representation. Starting from the original idea of the *snakes* [5], Caselles *et al.* [6] derived the *geodesic active contours* for implementation using level set, which improved the performance of the initial level set by attracting the evolving contour using image gradients. The contour size and topology changes are easily handled using implicit representation of level set. Later, Chan and Vese [7] solved the Mumford–Shah functional [8] using level sets, which led to a region-based segmentation method called *active contour without edges*. With this method, object boundaries that are not necessarily defined by edges can be segmented. Another main result of this method is that regions can be conveniently represented using level set functions. With this new representation, a number of region-based segmentation methods and shape modeling approaches can be easily implemented using level set.

When segmenting or localizing an anatomical structure, prior knowledge is usually very helpful. Since the anatomic knowledge of the structures to be segmented is generally available, some approaches have been proposed to utilize this information to improve the robustness of medical image segmentation. Coostes *et al.* [9] made a breakthrough by constructing statistical shape models using corresponding points across a set of training images for image segmentation. Staib and Duncan [10] incorporated global shape information into the segmentation process by using an elliptic Fourier decomposition of the boundary and placing a Gaussian prior on the Fourier coefficients. Shen and Davatzikos [11] proposed an adaptive-focus statistical model that allows the deformation of the active contour in each stage to be influenced primarily by the most reliable matches. Later, Leventon *et al.* [12] incorporated statistical shape priors into the evolution process of geodesic active contours [6] by embedding each shape in the training data set as the zero level set. Rousson *et al.* [13], [14] derived a unified implicit representation to incorporate prior knowledge into region-based image segmentation process.

While most deformable model-based methods used in medical image segmentation involve only one contour at a time, not much attention has been paid to segmentation of multiple structures simultaneously using more than one deformable model. For instance, Zhu and Yuille [15] proposed an unsupervised classification model incorporated with region competition. Multiple regions are segmented by evolving a parametric active contour according to local region intensities. Zimmer and Olivio-Martin [16] used coupled parametric active contours to segment and track nonoccluding but in contact objects.

By using level sets, Zhao *et al.* [17] modeled the multiphase evolution in the field of fluid mechanics. Later, Samson *et al.* [18] applied this study to piecewise constant image segmentation. The study was further improved by [19]–[24]. Barra and Boire [20] designed 3-D fuzzy maps for encoding relative positions between anatomical structures. Probabilistic fuzzy logic was then incorporated into the segmentation process to achieve better performance. Mansouri *et al.* [21] represented structures using not only the regions enclosed by their own contours, but also the regions enclosed by the contours of other structures. Using this representation, the competition between the regions is considered when the contours evolve simultane-

ously. However, the numbering sequence of the regions may introduce bias to the segmentation results, since the representation of each region always depends on the region enclosed by those contours with lower numbers. Pitiot *et al.* [24] employed distance maps for adding distance constraints between anatomical structures into the segmentation process. However, the approaches in these studies only rely on image information and some relative position information, while shape priors of the structures are not considered.

A very relevant study to this paper is the study by Yang *et al.* [25], who introduced neighbor-constrained 3-D segmentation using a level-set-based deformable model. They constructed the joint density function of neighboring objects from a training set and estimated the shapes of the objects using a MAP framework with neighbor prior constraint. A similar idea was also independently exploited by Tsai *et al.* [26] and Litvin and Karl [27]. Using these models, multiple structures can be segmented simultaneously. However, only the global relative position information of neighboring contours is captured. Therefore, the neighboring contours may intersect (i.e., overlap) with each other under some conditions. In addition, the shape contours evolve independently, which makes it very difficult to remove the overlaps once they are generated during shape estimation.

III. MODEL OF INTERACTION

Consider an image I that has M structures of interest S_i ($i = 1, \dots, M$), which may come in contact with each other and have similar intensities or textures. Due to partial volume effects, the boundaries may be blurred, which causes many segmentation methods to fail. While in previous methods, contours evolve independently according to the image features, geometric curvatures, and shape priors of each structure, the unclear boundaries between these structures may cause problems including overlapping and leaking. To deal with these problems, we integrate the interaction between evolving neighboring curves and their shape priors into the segmentation process.

In our approach, curves C_i ($i = 1, \dots, M$) evolve simultaneously to approach the contours of the structures. Each structure S_i has its own shape estimate \hat{C}_i (estimation details are given in Section III-B), which helps to guide the evolution of the curve C_i in the segmentation process.

A. Interactive Contour Evolution

In this paper, the interaction mainly involves three types of actions, *attraction*, *repulsion*, and *competition* between neighboring shape contours. They are defined as follows.

To realize the interaction model, the attraction, repulsion, and competition forces are formulated by an energy functional. Neighboring structures are segmented simultaneously by minimizing the joint energy functional.

- 1) *Attraction*: It is commonly accepted that when segmenting an anatomical structure, having prior information of that structure can improve the segmentation result. Thus, attraction is introduced, which defines the force of attracting the evolving contour C_i toward its *a priori* shape estimate \hat{C}_i as shown in Fig. 1(a). Let $\{A_i | i = 1, 2, \dots, M\}$ and

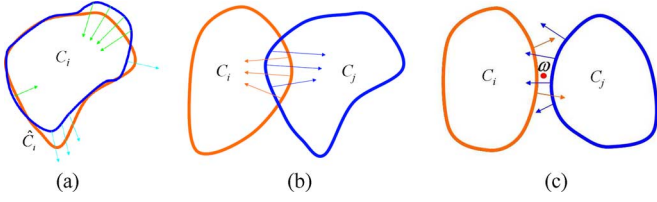


Fig. 1. Illustration of the interaction model. (a) Attraction: The contour C_i is attracted to its shape estimate \hat{C}_i . (b) Repulsion: The contours C_i and C_j push each other away in order to avoid overlapping. (c) Competition: The contours C_i and C_j compete for the unit ω .

$\{\hat{A}_i | i = 1, 2, \dots, M\}$ denote the areas enclosed by curves C_i and \hat{C}_i , respectively. The attractive force tends to minimize the difference between C_i and \hat{C}_i , which is equivalent to minimizing the nonoverlapping area between A_i and \hat{A}_i , i.e.

$$\arg \min \bigcup_i A_i \oplus \hat{A}_i \quad (1)$$

where the operator \oplus returns the difference between A_i and \hat{A}_i .

In our scheme, the attraction energy is formulated as follows:

$$E_{\text{attraction}} = \sum_{i=1}^M \xi_i A_i \oplus \hat{A}_i \quad (2)$$

where the positive parameter ξ_i controls the influence of its own shape estimate of the object contour C_i .

- 2) *Repulsion*: Since neighboring structures should not have overlapping areas, i.e.

$$\bigcup_{i \neq j} A_i \cap A_j = \emptyset \quad (3)$$

the repulsion between these curves must be emphasized to assure that the shape curves do not “enter” each other as shown in Fig. 1(b). The repulsion force can be naturally expressed as

$$\arg \min \bigcup_{i \neq j} A_i \cap A_j \quad (4)$$

where the operator \cap returns the area common to A_i and A_j .

Similar to attraction, the repulsion can be formulated as

$$E_{\text{repulsion}} = \sum_{i=1}^M \sum_{j=1, j \neq i}^M \omega_{ij} A_i \cap A_j \quad (5)$$

where the positive parameter ω_{ij} controls the repulsive force on the i th object from the j th object during the segmentation process.

- 3) *Competition*: Consider a unit area ω of the region near the boundaries of the structures to be segmented. An important question here is: “which structure does this unit belong to?” [see Fig. 1(c)]. The answer to this question relates to the issue of competition among these shape contours. Since a unit can only be enclosed by one contour at a time,

the decision is made by computing the probability of ω belonging to each structure

$$C_i^* = \arg \max_i p(\omega, C_i) = \arg \max_i p(\omega | C_i) p(C_i). \quad (6)$$

Different probability distribution functions (PDFs) can be selected depending on applications. Here, we assume each region is homogeneous so that the probability of $p(\omega | C_i)$ is formulated by Gaussian distribution as

$$p(\omega | C_i) = \frac{1}{\sqrt{2\pi}\sigma} \exp\left(-\frac{(I_\omega - c_i)^2}{\sigma^2}\right) \quad (7)$$

where I_ω is the intensity of ω , σ is the standard deviation of pixel intensities of the object, and c_i is the mean intensity value of the area enclosed by the contour C_i . It is worth noting that a more sophisticated PDF may be used if the image region is not homogeneous such as when it contains textures. The probability of observing a curve C_i is formulated as $\exp(-\mu L_i)$, where μ is a fixed positive parameter and L_i is the length of the curve.

Let $I : [0, a] \times [0, b] \rightarrow \mathbf{R}^+$ denote a given target image for segmentation. By taking negative logarithm of (6) and ignoring the constant terms, we have

$$E_{\text{competition}} = \lambda_o \sum_{i=1}^M \int_{in(C_i)} |I - c_i|^2 dx dy + \lambda_b \int_{\Omega_b} |I - c_b|^2 dx dy + \mu \sum_{i=1}^M \oint_{Q_i} dq \quad (8)$$

which assumes that each region consists of two homogeneous areas, i.e., object and background. c_i and c_b in (8) are the means of the object and the background areas in the i th region, respectively. λ_o and λ_b are fixed weighting parameters. It is noted that the first two terms in (8) are actually the same as the ones used in the well-known Mumford–Shah model [8], when $p(\omega | C_i)$ in (7) is formulated as a Gaussian distribution.

Combining the aforesaid terms, we obtain a joint energy functional for segmentation of multiple neighboring structures. The overall energy functional E is defined as

$$\begin{aligned} E &= E_{\text{attraction}} + E_{\text{repulsion}} + E_{\text{competition}} \\ &= \sum_{i=1}^M \xi_i A_i \oplus \hat{A}_i + \sum_{i=1}^M \sum_{j=1, j \neq i}^M \omega_{ij} A_i \cap \hat{A}_j \\ &\quad + \lambda_o \sum_{i=1}^M \int_{in(C_i)} |I - c_i|^2 dx dy \\ &\quad + \lambda_b \int_{\Omega_b} |I - c_b|^2 dx dy + \mu \sum_{i=1}^M \oint_{Q_i} dq. \end{aligned} \quad (9)$$

The segmentation is achieved by minimizing the aforementioned functional. In this paper, we use multiple-level sets scheme for energy minimization, which is detailed in Section IV-A.

B. Interactive Shape Prior Estimation

To incorporate the shape prior information into the segmentation process, we consider a probabilistic approach, and compute shape prior with a set of given training instances. To build the shape model, we choose a representation of shapes, and then define a probability density function over the parameters of the representation.

Let $\mathbf{C} = \{\mathcal{C}_i | i = 1, 2, \dots, n\}$ of n denote a set of registered training shapes (obtained by rigid registration). In order to incorporate the influence of the prior shape model to the evolution process as in (28), the shape and the pose of each model must be correctly estimated. Let $\hat{\Psi}_i$ denote the estimated region of the i th object. At each step of the curve evolution, it is estimated by

$$\hat{\Psi}_{i\text{MAP}} = \arg \max_{\hat{\Psi}_i} p(\hat{\Psi}_i | \Psi_i, \hat{T}_i, \nabla I) \quad (10)$$

where $\hat{T}_i = \{\hat{\Psi}_k | 1 \leq k \leq M \text{ and } k \neq i\}$ and ∇I represents the image gradients. To compute the MAP curve, we expand (10) using Bayes' Rule

$$p(\hat{\Psi}_i | \Psi_i, \hat{T}_i, \nabla I) = \frac{p(\Psi_i, \hat{T}_i | \hat{\Psi}_i) p(\nabla I | \Psi_i, \hat{T}_i, \hat{\Psi}_i) p(\hat{\Psi}_i)}{p(\Psi_i, \hat{T}_i, \nabla I)}. \quad (11)$$

When computing the MAP shape estimate in (10), the normalization term in the denominator of (11) can be discarded, since it does not depend on the estimated shape of the i th object.

In addition, when we estimate the priori shape $\hat{\Psi}_i$ of the i th structure, the current i th contour Ψ_i and other shape estimates \hat{T}_i are considered to be fixed in this step. Thus, there is no interaction between them and then we have

$$p(\Psi_i, \hat{T}_i | \hat{\Psi}_i) = p(\Psi_i | \hat{\Psi}_i) \prod_{k=1, k \neq i}^M p(\hat{\Psi}_k | \hat{\Psi}_i) \quad (12)$$

where

$$p(\Psi_i | \hat{\Psi}_i) = \exp(-\alpha A_i \oplus \hat{A}_i) \quad (13)$$

$$p(\hat{\Psi}_k | \hat{\Psi}_i) = \exp(-\beta \hat{A}_k \cap \hat{A}_i) \quad (14)$$

and α, β are positive weights.

The second term in the numerator of (11) computes the probability of seeing certain image gradients given the current curve and the estimated curves. Since the gradient is a local feature, it is reasonable to assume that this probability does not depend on other estimated curves. Thus, we have

$$p(\nabla I | \Psi_i, \hat{T}_i, \hat{\Psi}_i) = p(\nabla I | \hat{\Psi}_i). \quad (15)$$

In the ideal case, the gradient should only be significant on the object contours, i.e., where $\Psi_i(x, y) = 0$. Thus, we only count the gradient magnitude on these contours when computing the probability. The gradient probability term is modeled as a Laplacian of the goodness of fitting the shape estimate to the gradient map

$$p(\nabla I | \hat{\Psi}_i) = \exp \left(-\gamma \sum_{\hat{\Psi}_i(x,y)=0} g(|\nabla I(x, y)|) \right) \quad (16)$$

where γ is a positive weight parameter and function $g(|\nabla I|)$ is defined as $1/(1 + |\nabla I|^2)$.

To avoid the point correspondence problem and to effectively add the *a priori* shape influence, each curve \mathcal{C}_i in the training set is represented implicitly by the zero level set of its signed distance map Ψ_i , which will be described in detail in Section IV-A. The mean and variance of the training data can be computed using *principal component analysis* (PCA) [12]. Subtracting the mean shape, $\bar{\Psi} = \frac{1}{n} \sum_{i=1}^n \Psi_i$, from each Ψ_i and reshaping the differences result in column vectors in a $(a \cdot b) \times n$ dimensional matrix \mathbf{P} . Using *singular value decomposition* (SVD), the matrix is decomposed as $\mathbf{P} = \mathbf{U}\mathbf{\Sigma}\mathbf{V}^T$. Matrix \mathbf{U} is the model with orthogonal column vectors that consist of the modes of shape variation, and diagonal matrix $\mathbf{\Sigma}$ is composed of the corresponding singular values, i.e., mode amplitudes. An estimate of the object shape can be represented by k principal components \mathbf{U}_k and a k -dimensional vector of shape parameter \mathbf{b} (where $k < n$) [12] as

$$\hat{\Psi} = \mathbf{U}_k \mathbf{b} + \bar{\Psi}. \quad (17)$$

Under the assumption of a Gaussian distribution of shape represented by \mathbf{b} , we can compute the probability of a certain curve as

$$p(\hat{\Psi}) = p(\mathbf{b}) = \frac{1}{\sqrt{(2\pi)^k |\mathbf{\Sigma}_k|}} \exp \left(-\eta \frac{1}{2} \mathbf{b}^T \mathbf{\Sigma}_k^{-1} \mathbf{b} \right) \quad (18)$$

where $\mathbf{\Sigma}_k$ contains the first k rows and k columns of $\mathbf{\Sigma}$, and η is a positive weight parameter.

By putting the results in (12)–(18) into the MAP estimation (11), the probability of shape estimates can be obtained. We then take negative logarithm to the equation and ignore the constant terms to get

$$E_i^{\text{MAP}} = \alpha A_i \oplus \hat{A}_i + \beta \sum_{k=1, k \neq i}^M \hat{A}_k \cap \hat{A}_i + \gamma \sum_{\hat{\Psi}_i(x,y)=0} g(|\nabla I|) + \eta \frac{1}{2} \mathbf{b}^T \mathbf{\Sigma}_k^{-1} \mathbf{b}. \quad (19)$$

The prior shape will be estimated by minimizing the energy in (19). The implementation details are given in Section IV-C.

IV. IMPLEMENTATION USING LEVEL SETS

In this section, we discuss the minimization of the energy functional (9) using level sets. Since contours evolve simultaneously, we propose using multiple level sets for contour representation to implement our segmentation method. The level set is chosen mainly due to its convenience of obtaining regions enclosed by the contours. In our implementation, signed distance transformation is chosen to generate the level set function. The areas enclosed by a contour have negative distance values while the outside areas have positive distance values. Therefore, regions enclosed by the contours can be easily retrieved by checking the sign of the voxel values. In addition, the implicit representation provided by level sets makes the implementation simple and effective, especially when extending the segmentation approach from 2-D to 3-D. We first present the

multiple level sets method and then derive the level sets evolution equation to minimize the energy functional (9). Finally, the MAP shape estimation for obtaining shape priors of the target structures is provided.

A. Level Set Representation

Multiple level sets were first used for computing multiphase motion by Zhao *et al.* [17]. In their study, a region Ω with smooth boundary can be implicitly represented by a level set function $\Psi(x, y)$ as

$$\begin{cases} \Psi(x, y) < 0, & \text{for } (x, y) \in \Omega \\ \Psi(x, y) = 0, & \text{for } (x, y) \in \partial\Omega \\ \Psi(x, y) > 0, & \text{for } (x, y) \in \overline{\Omega^c}. \end{cases} \quad (20)$$

According to this equation, a level set function is in fact an effective region descriptor. Therefore, we use the same symbol Ψ as in the previous section to denote both region and level set function. Using the level set representation, the length L of the boundary $\partial\Omega$ and the area A of the region Ω can be computed by

$$L(\partial\Omega) = \int_{\Omega} |\nabla\Psi(x, y)|\delta(\Psi(x, y)) dx dy \quad (21)$$

and

$$A(\Omega) = \int_{\Omega} H(\Psi(x, y)) dx dy \quad (22)$$

respectively, where $H(x)$ is the Heaviside function

$$H(x) = \begin{cases} 1, & x \leq 0 \\ 0, & x > 0 \end{cases} \quad (23)$$

and $\delta(x)$ is the Dirac delta function

$$\delta(x) = \frac{d}{dx}H(x). \quad (24)$$

B. Evolution of Multiphase Level Sets

In our level set formulation, C_i denotes the contour of the i th object being segmented, which is embedded as the zero level set of a level set map Ψ_i defined in (20), i.e., $C_i(t) = \{(x, y) | \Psi_i(x, y, t) = 0\}$. The signed distance transform is used to generate the level set function Ψ_i according to contour C_i . Ψ_i is defined to be positive outside C_i and negative inside C_i . Each of the M objects being segmented in the image has its own contour C_i and corresponding Ψ_i .

The energy functional (9) is formulated in the level set framework by using regularized versions of the Heaviside function H in (23) and the Dirac function δ in (24), which are denoted by H_ε and δ_ε , respectively, and are defined as follows:

$$H_\varepsilon(z) = \frac{1}{2} \left(1 + \frac{2}{\pi} \arctan \left(\frac{z}{\varepsilon} \right) \right) \quad (25)$$

and

$$\delta_\varepsilon(z) = \frac{d}{dz}H_\varepsilon(z) = \frac{\varepsilon}{\pi(\varepsilon^2 + z^2)}. \quad (26)$$

Using the level set representation in IV-A, we have

$$\begin{aligned} E = & \xi \sum_{i=1}^M \int_{\Omega} \{(1 - H_\varepsilon(\Psi_i(x, y)))H_\varepsilon(\hat{\Psi}_i(x, y)) \\ & + H_\varepsilon(\Psi_i(x, y))(1 - H_\varepsilon(\hat{\Psi}_i(x, y)))\} dx dy \\ & + \omega \sum_{i=1}^M \sum_{j=1, j \neq i}^M \int_{\Omega} H_\varepsilon(\Psi_i(x, y))H_\varepsilon(\Psi_j(x, y)) dx dy \\ & + \lambda_o \sum_{i=1}^M \int_{\Omega} |I(x, y) - c_i|^2 H_\varepsilon(\Psi_i(x, y)) dx dy \\ & + \lambda_b \int_{\Omega} |I(x, y) - c_b|^2 \prod_{i=1}^M (1 - H_\varepsilon(\Psi_i(x, y))) dx dy \\ & + \mu \sum_{i=1}^M \int_{\Omega} |\nabla\Psi_i(x, y)|\delta_\varepsilon(\Psi_i(x, y)) dx dy \end{aligned} \quad (27)$$

where Ω denotes the image domain. Keeping each c_i and also c_b fixed and minimizing energy E in (27) with respect to $\Psi_i(x, y)$ ($i = 1, 2, \dots, M$), the associated Euler–Lagrange equation for each unknown level set function $\Psi_i(x, y)$ is deduced. After parameterizing the descent direction by an artificial time $t \geq 0$, the evolution equation in each $\Psi_i(t, x, y)$ is

$$\begin{aligned} \Delta\Psi_i = & \delta_\varepsilon(\Psi_i) \left(\xi(2H_\varepsilon(\hat{\Psi}_i) - 1) - \omega \sum_{j=1, j \neq i}^M H_\varepsilon(\Psi_j) \right. \\ & \left. - \lambda_o |I - c_{1i}|^2 - \mu \operatorname{div} \left(\frac{\nabla\Psi_i}{|\nabla\Psi_i|} \right) \right. \\ & \left. + \lambda_b \prod_{j=1, j \neq i}^M (1 - H_\varepsilon(\Psi_j)) |I - c_{2i}|^2 \right). \end{aligned} \quad (28)$$

Due to the presence of the Dirac function δ_ε , whose width depends on the value of ε , a “natural” narrow-band level set evolution equation (28) is obtained [28]. Thus, only pixels of the level set maps falling in the narrow bands need to be updated in each iteration, which can greatly reduce the computational complexity.

C. Estimation of Shape Priors

Following the derivation in Section III-B, the shape estimation equation (19) can be implemented by representing the regions using level sets

$$E_i^{\text{MAP}} = E_{i1}^{\text{MAP}} + E_{i2}^{\text{MAP}} \quad (29)$$

where

$$\begin{aligned} E_{i1}^{\text{MAP}} = & \alpha \int_{\Omega} \{(1 - H_\varepsilon(\Psi_i))H_\varepsilon(\hat{\Psi}_i) \\ & + H_\varepsilon(\Psi_i)(1 - H_\varepsilon(\hat{\Psi}_i))\} dx dy \\ & + \beta \sum_{j=1, j \neq i}^M \int_{\Omega} H_\varepsilon(\hat{\Psi}_i)H_\varepsilon(\hat{\Psi}_j) dx dy \\ & + \gamma \int_{\Omega} \delta_\varepsilon(\hat{\Psi}_i)g(|\nabla I|) dx dy \end{aligned} \quad (30)$$

and

$$E_{i2}^{\text{MAP}} = \eta \mathbf{b}^T \Sigma_k^{-1} \mathbf{b}. \quad (31)$$

The shape estimation energy in (29) is then minimized in two steps. We first minimize the energy E_{i1}^{MAP} by using the gradient descent method according to

$$\begin{aligned} \Delta \hat{\Psi}_i = \delta_\varepsilon(\hat{\Psi}_i) & \left(\alpha(2H_\varepsilon(\Psi_i) - 1) - \beta \sum_{j=1, j \neq i}^M H_\varepsilon(\hat{\Psi}_j) \right. \\ & \left. + \gamma \nabla \hat{\Psi}_i \cdot \nabla g(|\nabla I|) \right). \end{aligned} \quad (32)$$

Since this shape estimation can be considered as a linear combination of several eigenshapes as in (17), we can compute the coefficients $\hat{\mathbf{b}}$ as

$$\hat{\mathbf{b}}_i = \mathbf{U}_{ik}^T (\hat{\Psi}_i - \bar{\Psi}_i). \quad (33)$$

The coefficients \mathbf{b} are further regularized by minimizing the second part of the MAP energy in (31) as

$$\Delta \mathbf{b}_i = -2\eta \Sigma_{ik}^{-1} \hat{\mathbf{b}}_i. \quad (34)$$

After computing $\mathbf{b}_i = \hat{\mathbf{b}}_i + \Delta \mathbf{b}_i$, the shape estimation can then be updated using (17).

D. Summary of the Proposed Algorithm

A summary of the implementation details of our approach presented in Sections IV-B and IV-C is given in Algorithm 1. In each main iteration, contours first evolve with fixed shape priors and then shape estimations are updated. The algorithm continues to iterate until the change of shapes in each iteration is lower than a given threshold, which is chosen empirically. In our study, the threshold is set as 0.02, which means that the segmentation will stop if only no more than 2% of the shape changes.

Algorithm 1 Segmentation of Neighboring Structures

Input: Image to be segmented and initial contours of each structure
- Initialize the shape prior estimations as mean *a priori* shapes
while Changes of contours are above the threshold **do**
 for $i = 1, \dots, M$ **do**
 - Evolve level set maps Ψ_i according to equation (28)
 end for
 for $i = 1, \dots, M$ **do**
 - Update shape estimate $\hat{\Psi}_i$ according to equation (32)
 - Compute \mathbf{b}_i using (33)
 - Regularize coefficients \mathbf{b}_i by computing $\Delta \mathbf{b}_i$ using (34)
 end for
end while

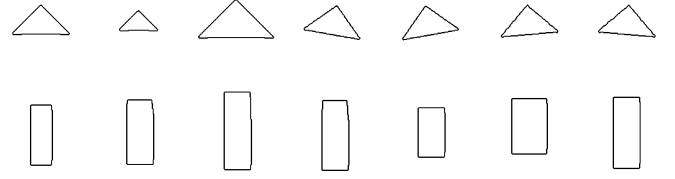


Fig. 2. Some training samples of the triangle and rectangle for the synthetic image segmentation.

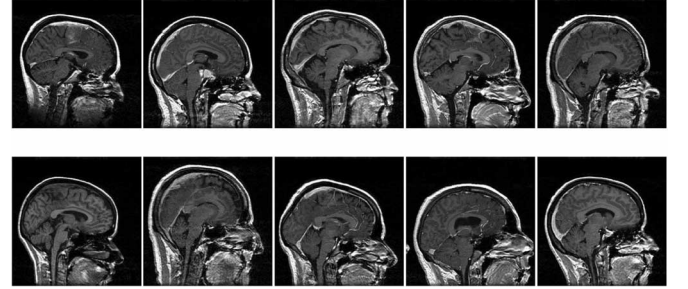


Fig. 3. 2-D sample slices of ten 3-D data volumes.

V. MATERIALS AND METHODS

A. Materials

1) *2-D Synthetic Images:* We tested our proposed segmentation algorithm on simple 2-D synthetic images shown in Fig. 2. In the 128×128 images to be segmented [see Fig. 4(a)], the two objects, which are made to share part of the boundary, have the same intensity in the range $[0, 255]$ and some Gaussian noise is added. For each object, a training set of 12 sample contours is used.

2) *2-D MR Brain Images:* The proposed method was applied to segmenting amygdala and hippocampus from ten 2-D brain MR T1 images (some sample images shown in Fig. 6). The images were obtained from a simulated brain database called BrainWeb [29]. The size of each image is 256×256 with spatial resolution of 1 mm^3 . The pixel intensity falls in the range of $[0, 255]$.

For every image, the following three cases are tested:

- 1) case *A*: without any *a priori* knowledge as an implementation of methods in [6] and Chan01;
- 2) case *B*: with only shape priors as an implementation of the method in [12];
- 3) case *C*: with the proposed model of interaction.

The same initial contour and parameter set are used for each case over the ten experiments.

3) *3-D MR Brain Images:* In our experiment on 3-D data, ten sets of MRI volume data containing brain tumor were used to test the method. The dimension of each volume is $256 \times 256 \times 124$ with voxel size of $0.9375 \times 0.9375 \times 1.5 \text{ mm}^3$ obtained with a GE 1.5T MR imaging device [30]. The voxel intensity falls in the range of $[0, 255]$. Sample 2-D slices extracted from the volumes are shown in Fig. 3.

Due to the deformation caused by brain tumors at different locations, there is obvious difference between the structures of

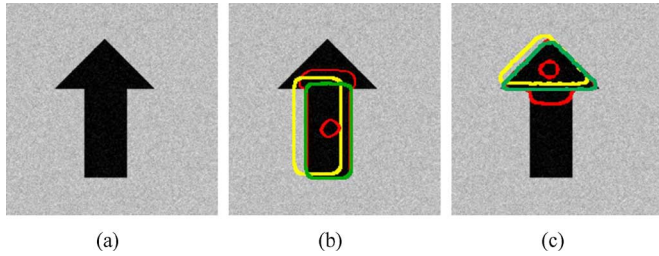


Fig. 4. Results without interaction ($\xi = 0.2$): (a) the original synthetic image, (b) the segmentation results for rectangle, (c) the results for triangle. Yellow curves represent the initial MAP shape. Green curves illustrate the final MAP shape. Red curves show the initial contours (small red circles) and final contours.

ventricles. This makes it difficult to accurately extract the left and right structures.

B. Evaluation Methods

Quantitative evaluation of segmentation results is an important step for validation of the proposed method [31], [32]. The “leave-one-out” cross-validation strategy is used for evaluation. When segmenting one image, we used the expert-drawn shapes of all the other images as the shape priors to build the statistical shape prior model.

To validate the results, the mean absolute distance is adopted as a metric to measure the difference between our segmentation results and the ground truth [33], [34]. In our paper, the manual segmentation results obtained by a radiologist were considered as the ground truth. The radiologist performed manual segmentation by drawing contours using a software tool.

There are several parameters to be set in our proposed segmentation algorithm. Parameter λ adjusts the contribution of the homogeneity of each region to the total energy and it can be assigned a large value if the region is piecewise smooth. Parameter μ controls the smoothness of the contours, ξ controls the attractive force from the estimated shape priors, and ω controls the repulsive force from other neighboring structures. The parameters ξ and ω should be given small values for robustness, since large values could abruptly change the shapes of the evolving contours. Based on empirical tests using a range of medical images, we found $\lambda_o = \lambda_b = 0.1$ and $\mu = 0.05$ to work very well in our experiments. The effects of varying the other two parameters ξ and ω are discussed in the following sections.

VI. EXPERIMENTAL RESULTS AND DISCUSSION

A. Evaluation of the Interaction Model by Simulations

Our method was first applied to 2-D synthetic images that consist of one black arrow composed of a triangle and a rectangle, with no defined boundaries between them as shown in Fig. 2. It is difficult to avoid leakage using only shape prior information as in [12]. Fig. 4 shows severe leakage as the contours of the triangle and rectangle leak into other’s regions. In Fig. 5, the interaction model is taken into account where the same parameters are adopted except $\omega = 0.3$, and leakage is avoided due to competition and repulsion between the two objects.

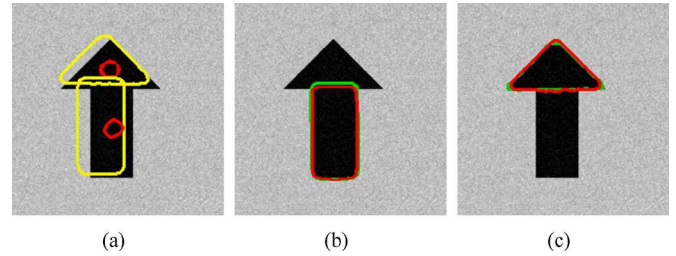


Fig. 5. Results with interaction. Parameters are the same as in Fig. 4, except $\omega = 0.3$: (a) the initial curves and estimated shapes, (b) the segmentation results of rectangle, (c) the results for triangle.

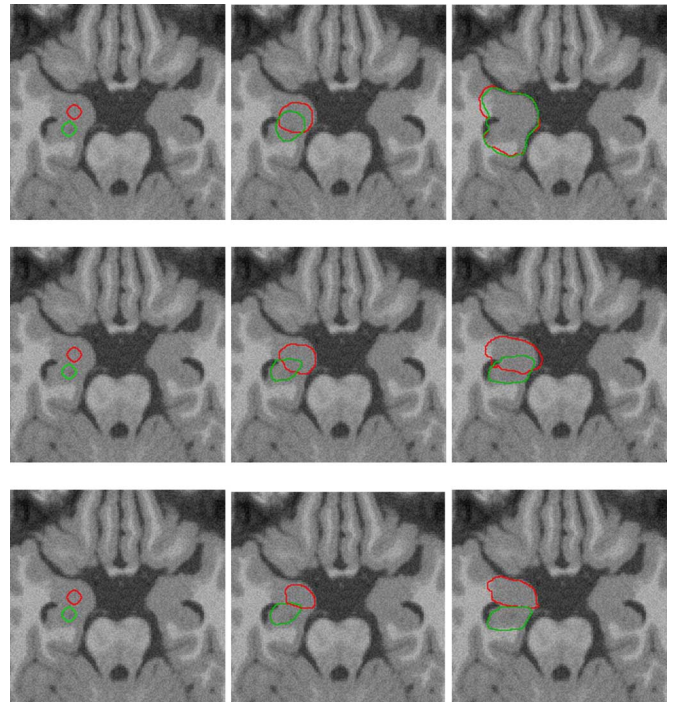


Fig. 6. Three steps in the segmentation of amygdala and hippocampus in a brain image [29]. (Top row): results of case A. (Middle row): results of case B with $\xi = 0.2$. (Bottom row): results of case C, where $\omega = 0.2$ and other parameters are the same as for the middle one. (The upper structure is object 1 and the lower one is object 2). The final segmentation results are shown in the third column, where the structures are correctly segmented only by employing the model of interaction.

B. Segmentation of Amygdala and Hippocampus

Segmentation of amygdala and hippocampus was performed on ten brain MR images. Fig. 6 shows the segmentation of the amygdala and hippocampus in a 2-D MR image. In Fig. 6, the first column shows the initial contours, the second the intermediate evolving contours, and the third the final segmentation results. The top row, which corresponds to case A, shows that finally the two evolving contours become one due to the extremely poorly defined boundaries and very similar intensities. The middle row shows the results for case B. It is clear that the final results, which incorporate the shape priors are more meaningful. However, there are some overlapping areas between the red and green contours due to the ill-defined boundaries. The overlapping is unavoidable unless the neighboring organ

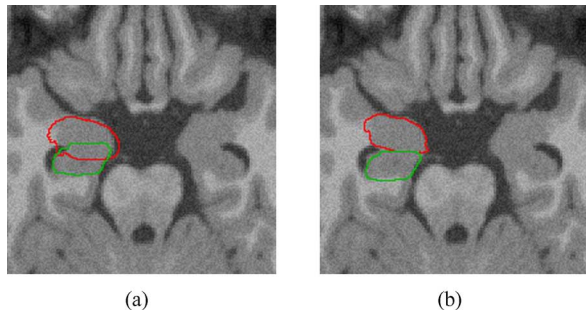


Fig. 7. MAP shape estimates of the images shown at the middle and bottom rows of Fig. 6. (a) MAP shape estimate with only individual prior shape information. (b) MAP shape estimate with the interaction between the two contours.

TABLE I
MEAN ABSOLUTE DISTANCE BETWEEN OUR SEGMENTATION RESULTS AND THE GROUND TRUTH (UNIT: PIXEL)

Case	Amygdala	Hippocampus
A	10.92	10.61
B	2.28	2.35
C	0.32	0.36

imposes a constraint on the evolution of the contour. The third row presents the results for case *C*. All parameters are the same as those in the middle row except $\omega = 0.2$. In the final results (the bottom right image of Fig. 6), the two structures are nicely segmented only when the interaction model is incorporated. We also note the overlap is avoided in the corresponding intermediate stage (the bottom image in column 2). Compared to the case when only *a priori* shape information (middle row) is used, our method does not produce overlapping contours.

In Fig. 7, we can see that the introduction of interaction between models into the multiple object segmentation process not only prevents overlapping of evolving neighboring contours but also benefits the shape estimation. With only shape priors, segmentation processes for each organ are treated independently. When leakage occurs (as in the second image of the middle row in Fig. 6), an incorrect MAP shape estimate will be obtained, which tends to misguide further evolution of the contour. The final MAP shape estimates are shown in Fig. 7(a). After incorporating interactions between models, evolution of the contours and MAP shape estimates tend to minimize the overlaps with other contours as well. Each shape estimate becomes less probable when it overlaps with others. Thus, as shown in Figs. 6 and 7, incorporating the interaction model both benefits the shape estimation and the contour evolution process and will, in turn, assist in obtaining good and robust segmentation results.

The mean absolute distance errors for amygdala and hippocampus under each case are shown in Table I. In case *A*, segmentation using only gray level information results in relatively large errors. This could be explained by severe leakage due to insufficient prior knowledge (as in the 1st row of Fig. 6). In case *B*, segmentation results are improved due to the guidance of shape priors (as in the 2nd row of Fig. 6). In case *C*, the results are further improved due to the employment of the model of interaction, which prevents overlapping and small leakage (as in the 3rd row of Fig. 6).

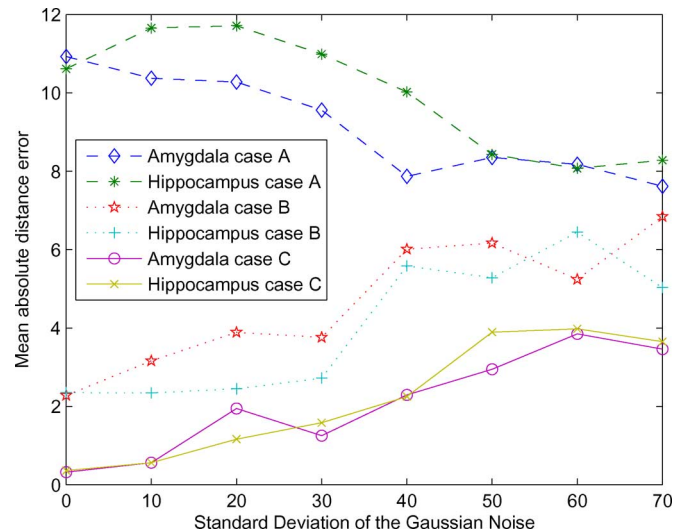


Fig. 8. Mean absolute distance for amygdala and hippocampus for the three cases in the presence of different levels of noise.

In order to test the robustness of our approach, we segment the amygdala and hippocampus MR data sets after adding Gaussian noise with different standard deviations. All the three cases of segmentation are involved in validating the results. Fig. 8 shows the mean absolute distance in the presence of different Gaussian noise. When the standard deviation is zero, the distances are the same as in Table I. As shown in Fig. 8, the segmentation performance improves when shape priors are used, while the method with the proposed interaction model obtains the smallest error among the three cases. As the standard deviation of the noise increases, the distances for cases *B* and *C* gradually increase. It is also interesting that the distances for case *A* decrease with noise. This could be explained as follows: for case *A*, as the segmentation process only uses gray-level information, this means that the contour propagation will slow down if edges are encountered. Due to the weak boundaries between the amygdala and hippocampus, severe leakage can happen even without the added noise (as shown in Fig. 6 and Table I). However, in the presence of added noise, false edges were introduced that can hinder the propagation process thus reducing severe leakage, which results in smaller distance errors.

Another factor in our algorithm, which may influence the segmentation results, is the initial seed points of level sets. To test the robustness of the algorithm with respect to the locations of the initial seeds, first, Gaussian noise with a variance of 30 is added to the images in the dataset. Then, we fix all the parameters except the location of the initial seeds. By varying the initial seed positions and comparing the results with the ground truth, we can obtain the mean absolute distances for each algorithm as shown in Fig. 9. It can be seen that the algorithms are not sensitive to the initial seed positions, while our approach has the smallest mean absolute distance to the ground truth. The 3-D segmentation results of amygdala and hippocampus are shown in Fig. 10.

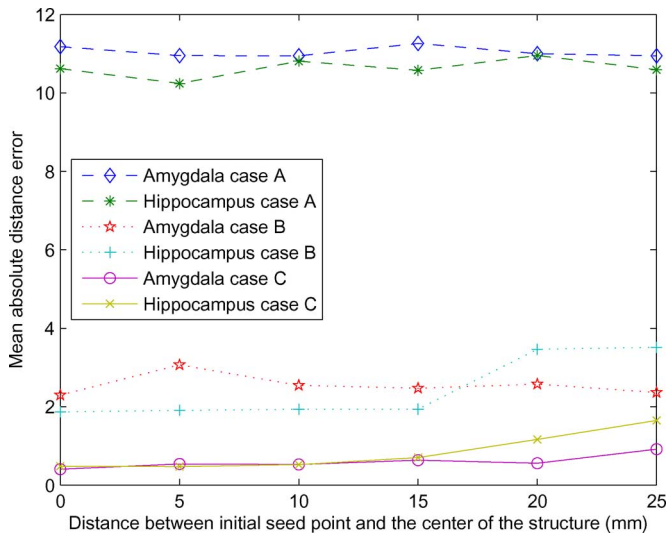


Fig. 9. Mean absolute distance under three cases with different locations of initial seed points for amygdala and hippocampus segmentation in the presence of noise.



Fig. 10. 3-D segmentation results of left (1st row) and right (2nd row) amygdala and hippocampus.

C. Segmentation of Lateral Ventricles

Since the structure contours are implicitly represented using level sets in our scheme, the proposed method can be directly used for segmentation of 3-D medical images. In this section, we demonstrate the segmentation of lateral ventricles in 3-D from MRI images. The segmentation of ventricles is important for accurate quantification of white matter lesions by reducing the misclassification of lesions caused by choroid plexus and partial volume artifacts at the surface of ventricles. The quantitative measurement, as well as 3-D display of ventricles using segmentation can be expected to be of value in differential diagnosis, disease characterization, and follow-up investigations. In these applications, it is also necessary to distinguish the left and right lateral ventricles. However, due to the similarity in intensity and the adjacency between them, it has been difficult to separate them. In this section, we demonstrate the application of the interaction model to solve the problem.

The segmentation results are drawn on 2-D slices and also visualized in 3-D in Fig. 11 for qualitative assessment. Due to the rather large variance of the shape and strong similarity in intensity between the structures, the parameters used were set to $\xi = 0.1$ and $\omega = 0.3$. To quantitatively assess the performance of the method, the mean absolute distance error between our 3-D segmentation results and the manual one obtained from radiologists was evaluated and is presented in Table II. From

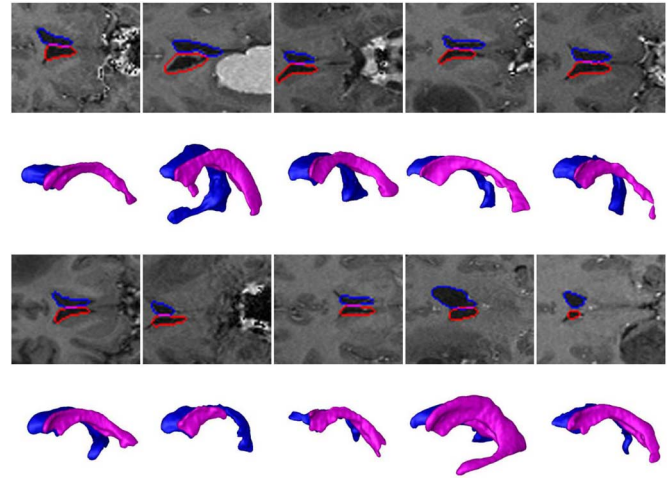


Fig. 11. Segmentation results of the left and right lateral ventricles. Odd rows: segmentation results overlaid on 2-D slices. Even rows: visualization of the 3-D segmentation results.

TABLE II
MEAN ABSOLUTE DISTANCE BETWEEN THE OBTAINED 3D SEGMENTATION RESULTS AND THE MANUAL SEGMENTATION RESULTS. (UNIT: VOXEL)

No.	1	2	3	4	5
Left	0.697	0.999	0.818	0.607	0.810
Right	0.659	1.196	1.053	0.668	0.683
No.	6	7	8	9	10
Left	0.808	0.873	0.740	0.522	0.728
Right	0.965	0.827	0.812	0.616	0.777

the results, it is clear that the lateral ventricles were accurately segmented and nicely separated into two parts. The average errors of the segmentation of left lateral and right lateral are 0.76 voxel and 0.826 voxel, respectively. The average overlay error is less than 1% of the size of the manually segmented structures.

VII. DISCUSSION AND CONCLUSION

In this paper, we propose a novel method that is able to effectively segment neighboring structures with similar texture and intensity. By intuitively describing the relationships between neighboring structures and their respective shape estimates, our method effectively models interaction between neighboring contours to enable extraction of the boundaries that separate them. Our approach also produces better results in situations where the prior shape information is not sufficient to achieve a good and robust boundary estimation due to the poorly defined boundaries and very similar intensities as compared to the approaches in [7] and [12]. Promising results were obtained when our proposed method was extended to segment 3-D medical images.

Our proposed approach requires *a priori* knowledge in the form of training images consisting of manual segmentation results for modeling the structures of interest. The training shapes should cover most variations of structure shapes for effective shape guidance. Otherwise, the shape priors may not be correctly estimated during segmentation, which may result in poor performance.

It is not necessary to strictly follow the exact parameter settings used in our experiments. There is no significant performance change (<5%) even when the parameters vary by up to 30%. Using a 1.2 GHz PC, our method takes about 25 s to perform 2-D segmentation and 3 min for 3-D segmentation. Furthermore, the interaction between neighboring structures could be enhanced by incorporating additional terms such as relative locations of anatomical structures considering mass effect and differences between area sizes. In our future study, it would also be interesting to extend the segmentation scheme to images and structures with more sophisticated intensity and shape distributions.

ACKNOWLEDGMENT

The authors would like to thank Prof. S.-C. Wang and Dr. B. Shuter of the Department of Diagnostic Radiology at the National University Hospital in Singapore for providing some of the data sets and manual segmentation results used in this study.

REFERENCES

- [1] D. L. Pham and P.-L. Bazin, "Simultaneous boundary and partial volume estimation in medical images," in *Proc. Med. Image Comput. Comput.-Assist. Interv.*, 2004, pp. 119–126.
- [2] P. Yan, W. Shen, A. A. Kassim, and M. Shah, "Segmentation of neighboring organs in medical image with model competition," in *Proc. Med. Image Comput. Comput.-Assist. Interv.*, vol. 1, J. Duncan and G. Gerig, Eds. Berlin/Heidelberg, Germany: Springer-Verlag, 2005, pp. 270–277.
- [3] S. Osher and J. A. Sethian, "Fronts propagating with curvature-dependent speed: Algorithms based on Hamilton–Jacobi formulations," *J. Comput. Phys.*, vol. 79, pp. 12–49, 1988.
- [4] R. Malladi, J. A. Sethian, and B. C. Vemuri, "Shape modeling with front propagation: A level set approach," *IEEE Trans. Pattern Anal. Mach. Intell.*, vol. 17, no. 2, pp. 158–174, Feb. 1995.
- [5] M. Kass, A. Witkin, and D. Terzopoulos, "Snakes: Active contour models," *Int. J. Comput. Vis.*, vol. 1, no. 4, pp. 321–331, 1987.
- [6] V. Caselles, R. Kimmel, and G. Sapiro, "Geodesic active contours," *Int. J. Comput. Vis.*, vol. 22, no. 1, pp. 61–79, 1997.
- [7] T. F. Chan and L. A. Vese, "Active contours without edges," *IEEE Trans. Image Process.*, vol. 10, no. 2, pp. 266–277, Feb. 2001.
- [8] D. Mumford and J. Shah, "Optimal approximation by piecewise smooth functions and associated variational problems," *Commun. Pure Appl. Math.*, vol. 42, pp. 577–685, 1989.
- [9] T. F. Cootes, C. J. Taylor, D. H. Cooper, and J. Graham, "Active shape models—Their training and application," *Comput. Vis. Image Understand.*, vol. 61, no. 1, pp. 38–59, Jan. 1995.
- [10] L. H. Staib and J. S. Duncan, "Boundary finding with parametrically deformable models," *IEEE Trans. Pattern Anal. Mach. Intell.*, vol. 14, no. 11, pp. 1061–1075, Nov. 1992.
- [11] D. Shen and C. Davatzikos, "An adaptive-focus deformable model using statistical and geometric information," *IEEE Trans. Pattern Anal. Mach. Intell.*, vol. 22, no. 8, pp. 906–913, Aug. 2000.
- [12] M. E. Leventon, W. E. L. Grimson, and O. Faugeras, "Statistical shape influence in geodesic active contours," in *Proc. IEEE Conf. Comput. Vis. Pattern Recognit.*, 2000, vol. 1, pp. 316–323.
- [13] M. Rousson and N. Prigios, "Shape priors for level set representations," in *Eur. Conf. Comput. Vis.*, 2002, vol. 2, pp. 78–92.
- [14] M. Rousson, N. Paragios, and R. Deriche, "Implicit active shape models for 3D segmentation in MR imaging," in *Proc. Med. Image Comput. Comput.-Assist. Interv.*, 2004, pp. 209–216.
- [15] S. C. Zhu and A. Yuille, "Region competition: Unifying snakes, region growing, and Bayes/MDL for multiband image segmentation," *IEEE Trans. Pattern Anal. Mach. Intell.*, vol. 18, no. 9, pp. 884–900, Sep. 1996.
- [16] C. Zimmer and J.-C. Olivo-Martin, "Coupled parametric active contours," *IEEE Trans. Pattern Anal. Mach. Intell.*, vol. 27, no. 11, pp. 1838–1842, Nov. 2005.
- [17] H.-K. Zhao, T. F. Chan, B. Merriman, and S. Osher, "A variational level set approach to multiphase motion," *J. Comput. Phys.*, vol. 127, pp. 179–195, 1996.
- [18] C. Samson, L. Blanc-Feraud, G. Aubert, and J. Zerubia, "A level set model for image classification," *Int. J. Comput. Vis.*, vol. 40, no. 3, pp. 187–197, 2000.
- [19] L. A. Vese and T. F. Chan, "A multiphase level set framework for image segmentation using the Mumford and Shah model," *Int. J. Comput. Vis.*, vol. 50, no. 3, pp. 271–293, 2002.
- [20] V. Barra and J.-Y. Boire, "Automatic segmentation of subcortical brain structure in MR images using information fusion," *IEEE Trans. Med. Imag.*, vol. 20, no. 7, pp. 549–558, Jul. 2001.
- [21] A.-R. Mansouri, A. Mitiche, and C. Vazquez, "Multiregion competition: A level set extension of region competition to multiple region image partitioning," *Comput. Vis. Image Understanding*, vol. 101, no. 3, pp. 137–150, Mar. 2006.
- [22] H. Delingette and J. Montagnat, "Shape and topology constraints on parametric active contours," *Comput. Vis. Image Understanding*, vol. 83, no. 2, pp. 140–171, Aug. 2001.
- [23] N. Paragios and R. Deriche, "Geodesic active contours and level sets for the detection and tracking of moving objects," *IEEE Trans. Pattern Anal. Mach. Intell.*, vol. 22, no. 3, pp. 266–280, Mar. 2000.
- [24] A. Pitiot, H. Delingette, P. M. Thompson, and N. Ayache, "Expert knowledge guided segmentation system for brain MRI," *NeuroImage*, vol. 23, pp. S85–S96, 2004.
- [25] J. Yang, L. Staib, and J. Duncan, "Neighbor-constrained segmentation with level set based 3-D deformable models," *IEEE Trans. Med. Imag.*, vol. 23, no. 8, pp. 940–948, Aug. 2004.
- [26] A. Tsai, W. Wells, C. Tempany, E. Grimson, and A. Willsky, "Mutual information in coupled multi-shape model for medical image segmentation," *Med. Image Anal.*, vol. 8, no. 4, pp. 429–445, 2004.
- [27] A. Litvin and W. C. Karl, "Coupled shape distribution-based segmentation of multiple objects," in *Proc. Inform. Process. Med. Imag.*, 2005, pp. 345–356.
- [28] J. A. Sethian, *Level Set Methods and Fast Marching Methods*. New York: Cambridge Univ. Press, 1999.
- [29] R.K.-S. Kwan, A. C. Evans, and G. B. Pike, "MRI simulation-based evaluation of image-processing and classification methods," *IEEE Trans. Med. Imag.*, vol. 18, no. 11, pp. 1085–1097, Nov. 1999.
- [30] S. K. Warfield, M. Kaus, F. A. Jolesz, and R. Kikinis, "Adaptive, template moderated, spatially varying statistical classification," *Med. Image Anal.*, vol. 4, pp. 43–55, 2000.
- [31] B. Berkels, A. Rätz, M. Rumpf, and A. Voigt, "Extracting grain boundaries and macroscopic deformations from images on atomic scale," *J. Sci. Comput.*, vol. 35, no. 1, pp. 1–23, 2008.
- [32] C. P. Loizou, C. S. Pattichis, M. Pantziaris, and A. Nicolaidis, "An integrated system for the segmentation of atherosclerotic carotid plaque," *IEEE Trans. Inform. Technol. Biomed.*, vol. 11, no. 6, pp. 661–667, Nov. 2007.
- [33] G. J. Klein, X. Teng, W. J. Jagust, J. L. Eberling, A. Acharya, B. W. Reutter, and R. H. Huesman, "A methodology for specifying PET volumes-of-interest using multi-modality techniques," *IEEE Trans. Med. Imag.*, vol. 16, no. 4, pp. 405–415, Aug. 1997.
- [34] C. Loizou, C. Pattichis, M. Pantziaris, T. Yllis, and A. Nicolaidis, "Snakes based segmentation of the common carotid artery intima media," *Med. Biol. Eng. Comput.*, vol. 45, no. 1, pp. 35–49, Jan. 2007.



Pingkun Yan (S'04–M'05) received the B.Eng. degree in electronics engineering from the University of Science and Technology of China, Hefei, China, in 2001, and the Ph.D. degree in electrical and computer engineering from the National University of Singapore, Singapore, in 2005.

He was a Research Associate with the Computer Vision Laboratory at the University of Central Florida (UCF), Orlando. He is currently a Senior Member, Research Staff at Philips Research North America. He is also with the School of Computer Science,

University of Central Florida. His current research interests include computer vision, pattern recognition, machine learning, and their applications to biomedical image analysis and image-guided interventions.

Dr. Yan is a member of the Medical Image Computing and Computer Assisted Intervention (MICCAI) Society. He received the MICCAI 2005 Student Award for the best presentation on image segmentation and analysis.



Ashraf A. Kassim (S'82–M'85) received the B.Eng. (first class honors) and M.Eng. degrees in electrical engineering from the National University of Singapore (NUS), Singapore, in 1985 and 1987, respectively, and the Ph.D. degree in electrical and computer engineering from Carnegie Mellon University, Pittsburgh, PA, in 1993.

Since 1993, he has been with the Electrical and Computer Engineering Department, NUS, where he is currently an Associate Professor and Vice Dean of Engineering Faculty. His current research interests

include image analysis, machine vision, and video/image processing and compression.



Weijia Shen received the B.Eng. degree from Xi'an Jiaotong University, Xi'an, China, in 2003.

Since 2003, he has been working toward the Ph.D. degree at the Electrical and Computer Engineering Department, National University of Singapore. His current research interests include image processing, machine vision, and machine learning.



Mubarak Shah (F'03) is the Agere Chair Professor of Computer Science in the School of Computer Science, University of Central Florida, Orlando, where he is also the founding Director of the Computer Vision Laboratory. He is a researcher in a number of computer vision areas.

Prof. Shah is a Fellow of the International Association of Pattern Recognition. He is an Editor of the international book series on "Video Computing," Editor-in-Chief of *Machine Vision and Applications*, and an Associate Editor of *ACM Computing Surveys*.

He was an Associate Editor of the IEEE TRANSACTIONS ON PATTERN ANALYSIS AND MACHINE INTELLIGENCE, and a Guest Editor of the special issue of the *International Journal of Computer Vision* on video computing. He was the recipient of numerous awards including the Pegasus Professor award, the IEEE Distinguished Visitor speaker for 1997–2000, the IEEE Outstanding Engineering Educator Award in 1997, the Harris Corporation's Engineering Achievement Award in 1999, the TOKTEN awards from the United Nations Development Programme in 1995, 1997, and 2000, the Teaching Incentive Program Award in 1995 and 2003, the Research Incentive Award in 2003, the Millionaires' Club awards in 2005 and 2006, the University Distinguished Researcher Award in 2007, and the Honorable mention for the International Conference on Computer Vision 2005. He was nominated for the Best Paper Award at the ACM Multimedia Conference in 2005.